Method for the accurate determination of two-photon transition frequencies as demonstrated with the cesium $6S_{1/2} \rightarrow 6D_{3/2}$ hyperfine transitions

Chia-Wei Chang (張家維),^{1,*} Bo-Wei Chen (陳伯煒)⁰,^{3,1,2,*} Wen-Chun Chen (陳玟君)⁰,¹ Ko-Han Chen (陳可翰) , 1,2,3 Taro Mashimo (真下太郎) , Tzu-Yu Shen (沈子淯) , Tzu-Yu Shen (沈子淯) Po-Cheng Chang (張博程), and Wang-Yau Cheng (鄭王曜), and Wang-Yau Cheng (鄭王曜), ¹Department of Physics, National Central University, Taoyuan City 32001, Taiwan ²Molecular Sciences and Technology, Taiwan International Graduate Program, Academia Sinica, National Central University, Taipei 115201, Taiwan ³Institute of Atomic and Molecular Science, Academia Sinica, Taipei 11529, Taiwan ⁴Advanced Technology Laboratory, Chunghwa Telecom Laboratories, Taoyuan City 32661, Taiwan ⁵Quantum Technology Center, National Central University, Taoyuan City 32001, Taiwan

(Received 12 March 2025; revised 10 September 2025; accepted 8 October 2025; published 18 November 2025)

An experimental setup for accurately determining the frequency of alkali-metal-atom two-photon transitions is proposed and demonstrated, with which we avoid laser modulation by an offset-locking technique; keep away collision shift via a high-vacuum pumping; compensate for Zeeman shift directly from the information of the spectral linewidth; remove residual Doppler background by the two-photon crossover spectra; observe the frequency reproducibility between normal days and aftershocks; and compare different approaches of counting laser frequencies, that is, different time bases from either a cesium atomic beam clock or a precalibrated rubidium clock. The frequency of cesium $6S_{1/2} \rightarrow 6D_{3/2}$ hyperfine transitions and the corresponding hyperfine constants are hence updated, which are both significant for improving the calculation precision of atomic parity nonconservation and for enhancing the accuracy of the two-photon transition-based optical clocks.

DOI: 10.1103/9jtf-dm2q

I. INTRODUCTION

Determining the hyperfine structure and frequency of alkali-metal-atom forbidden transitions accurately is important for testing physical laws [1,2] and in metrology applications [3-5]. Determining the frequency of cesium M1and E2 transitions is particularly significant in the atomic parity-nonconservation (APNC) calculation [6-8], since the calculation needs the experimental knowledge of the relevant level energies (frequencies) to compose a suitable wave function via the B-spline technique in many-body perturbation theory [9]. To date, the calculation on cesium atoms yields the best APNC precision among all high-Z (atomic number) candidate atoms [10]. From the perspective of metrology applications, hot-atom-based alkali-metal two-photon transitions have been confirmed to be suitable optical frequency references [3-5] at different wavelength regimes. This is because the nonlinear dipole oscillation of the alkali-metal atoms is easier to induce, due to which the related spectrum yields a sufficient signal-to-noise ratio (SNR) for laser stabilization via a photon-multiplier tube (PMT). On the other hand, the single electron in the loosely bound excited state of the alkali-metal atoms is sensitive to the surroundings, such as the residual magnetic field and collisions with helium atoms diffusing from the atmosphere [4]. Taking the rubidium

 $5S_{1/2} \rightarrow 5D_{5/2}$ 778-nm clock transition as an example, the fractional laser frequency instability $\Delta f/f$ could reach the level of 10^{-15} [11] due to its high SNR and narrow spectral linewidth; however, the international frequency accuracy comparisons remain two to three orders of magnitude worse than the frequency precision (instability) [3]. The other twophoton transition-based frequency references show the same problem [4,5]. A scheme with detailed interpretations is presented in this paper to demonstrate that the accuracy problem mentioned above can be improved. In other words, we not only report an accurate cesium eigenvalue for the study of APNC but also demonstrate a general method to realize a twophoton transition-based optical clock where the major causes for the frequency inaccuracy are either avoided or reduced to an ignorable level.

II. EXPERIMENTAL SETUP

A. Modulation-free spectra and comb-laser-based spectrometer

Modulating the laser frequency not only loses the laser coherence but also leads to a modulation broadening [12]. Since the linewidth measurement performed in this paper plays a key role in judging the frequency accuracy of the spectrum of interest, modulation broadening is very unwelcome in precisely knowing the spectral linewidth. Moreover, the modulation shift, caused by residual amplitude modulation, nonlinear modulation, and an imperfect balanced mixer in the demodulation process, quite easily happens when the laser is in a high modulation width (depth) for obtaining a high SNR

^{*}These authors contributed equally to this work.

[†]Contact author: wycheng@phys.ncu.edu.tw

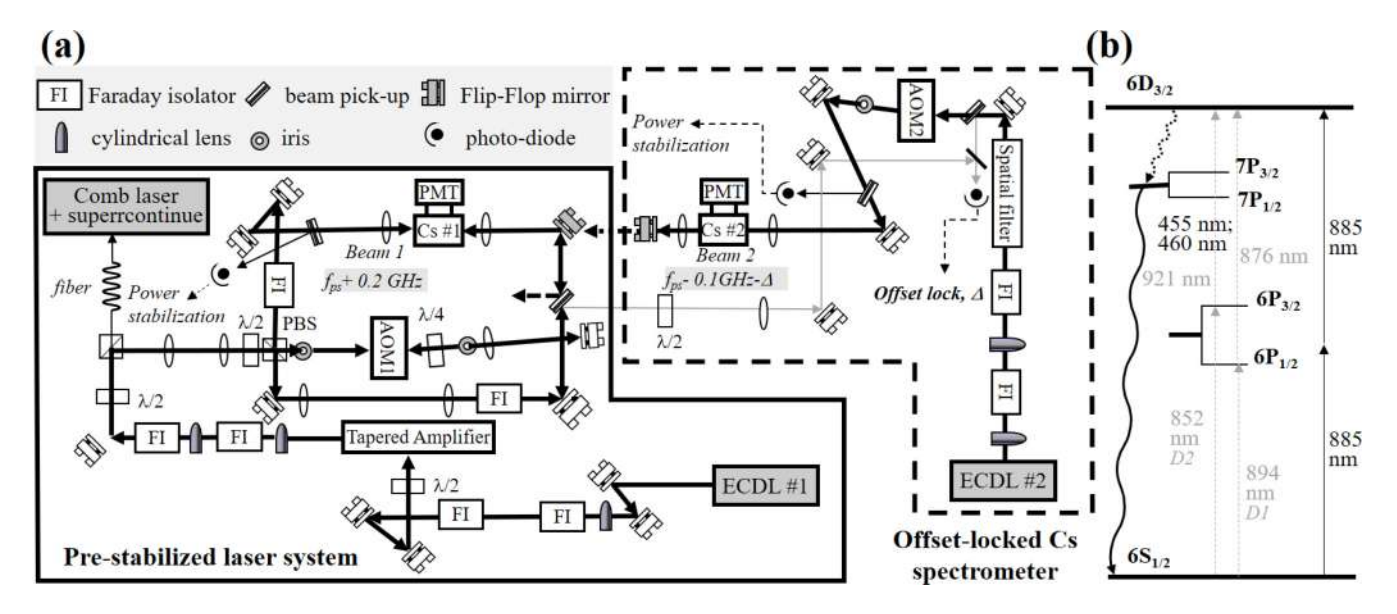


FIG. 1. Setup for a high-accuracy Cs spectrometer. (a) Schematic diagram: ECDL, extended-cavity diode laser; PBS, polarization beam splitter; f_{ps} , frequency of prestabilized laser; Δ , value of offset frequency; beam 1 and beam 2, see Sec. II D for details; Helmholtz coils for Cs #2 vacuum cell are not shown in the schematic. (b) Simplified level diagram relevant to the Cs spectrometer: solid line, laser light; dashed line, Cs D1 and D2 transitions; solid wavy line, blue fluorescence for the spectral signal detection. Hyperfine levels are not presented; see Fig. 2 and the text for details.

[13,14], which will also degrade the accuracy of an optical clock. Notwithstanding, modulating a laser and retrieving a derivative signal from a lock-in amplifier is still the most popular approach for laser stabilization. Therefore, in this paper we modulate the laser frequency to stabilize the extended-cavity diode laser (ECDL) #1 in Fig. 1, but determine the transition frequencies separately with the unperturbed spectra resolved by ECDL #2.

To prepare a cesium two-photon stabilized light source without laser modulation, we designed an optical layout as displayed in Fig. 1(a), where the solid and dashed insets contain a prestabilized laser system (PSLS) and a frequency offset-locked Cs spectrometer (OLCS), respectively. The OLCS was built to realize high-frequency accuracy and unperturbed cesium spectra for determining both the linewidths and the frequencies of cesium $6S_{1/2}$ - $6D_{3/2}$ hyperfine transitions. The relevant level diagram is illustrated in Fig. 1(b), in which the fluorescence from 7P to 6S was detected by a PMT as evidence of two-photon absorption. The detection area of the PMT is 1 in. Two homebuilt extended-cavity diode lasers (ECDL #1 and ECDL #2) having 25 and 70 mW output powers were implemented in the PSLS and the OLCS, respectively. The laser power after the tapered amplifier in the PSLS was 225 mW and was then divided into three optical paths, where 10 mW of power was sent to beat against one Ti:S comb-laser mode that was generated from a supercontinuum fiber, by which the frequency of the transverse axis in Fig. 2 was always calibrated. A polarization beam splitter in Fig. 1 divides the other laser beam into two optical paths: One portion of laser light goes through a double-pass acousticoptical modulator (AOM1) (+1 order was used). The AOM1 was driven with an average frequency of 100 MHz as the driving frequency was dithered from 99 MHz to 101 MHz at a dither frequency of 10 kHz. To avoid any additional amplitude modulation during dithering the AOM, we performed laser power stabilization using a beam pickup and a proportional integral loop whose electronic bandwidth (approximately $100 \, \text{kHz}$) was much larger than the dither frequency ($10 \, \text{kHz}$). Eventually, we prepared a $50 \pm 0.01 \, \text{mW}$ laser power in front of one commercial glass cesium cell (Cs #1). The power of the

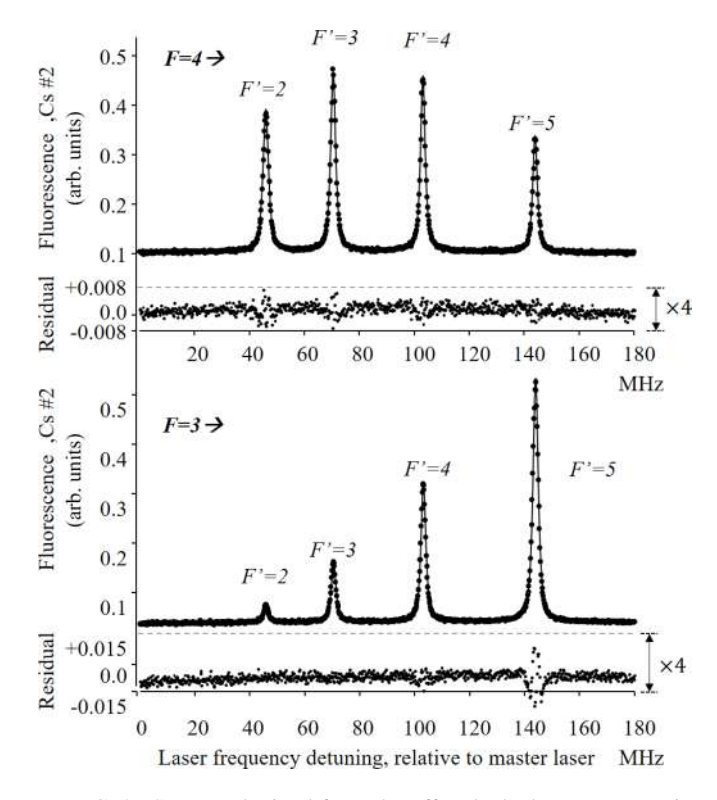


FIG. 2. Spectra obtained from the offset-locked spectrometer in Fig. 1. dots, data points with 1-s sampling time and 200 kHz per step; curve, multipeak Lorentian transit-time [17] fitting. The fitting residual is magnified four times.

TABLE I. Fitting results for the black spectra in Fig. 3.

$F = 4 \rightarrow$	F=2'	F = 3'	F = 4'	F=5'
Frequency shift (MHz)	2.13(3)	2.18(2)	2.11(2)	2.15(3)
Linewidth (MHz)	11.0(2)	11.0(2)	11.0(2)	10.9(3)

other counterpropagating laser beam in front of the other side of Cs #1 was 110 mW, which was frequency unmodulated. A small portion (10 mW) of the unmodulated laser beam, colored in gray, was sent to beat against ECDL #2 to perform frequency offset locking [15]. The amplitude-modulated fluorescence from PMT #1 was sent to a lock-in amplifier to prestabilize the frequency of ECDL #1. Consequently, a laser frequency instability of 3×10^{-13} fractional Allan deviation at an integrating time of 200 s was achieved, which is similar to the result of our previous work [16], while it is worse at short sampling time, as will be discussed in Sec. IIF. After avoiding modulation shift and suppression of collision shift and Zeeman shift, which will be discussed in Sec. II, a typical hyperfine structure resolved via the high-vacuum cesium cell #2 (Cs #2) is displayed in Fig. 2, where the frequency accuracy of the transverse axis is limited not by the frequency instability of the prestabilized laser but by the frequency accuracy of the comb laser. The transition frequency of each hyperfine component is fitted by a multipeak Lorentzian transit-time function [17] and the transition frequency of each hyperfine component is thus revealed. In Fig. 2 the fitting residual is magnified four times, from which a small background is perceived and is believed to result from the residual Doppler background (RDB), as will be discussed in Sec. II D and in Appendix A. Two flip-flop mirrors (gray color) in Fig. 1 could be flipped down so that the mutual counterpropagating beams in Cs cell #1 have different frequencies, by which we demonstrated an alternative to eliminate the RDB. This approach is addressed in detail in Sec. II D.

B. Keeping away collision shift with high vacuum

Our previous study [4] proved that atmospheric helium could penetrate a commercial Pyrex cell at approximately 0.22 mTorr/yr, which led to a 9-kHz/yr frequency shift for cesium 6S-8S hyperfine transitions. In the same experiment and with the same Cs cell, the 6S-6D transition was found to be three times more sensitive to helium collisions than the 6S-8S transition [4]. Table I reveals the helium collision shift and broadening according to the experimental data in Fig. 3. A multipeak Voigt function is used to fit the black data in Fig. 3, from which we deduce a 133(2) kHz/mTorr frequency shift and a linewidth broadening rate of 0.7(1) MHz/mTorr. This recently discovered error source motivated us to measure the transition frequency of the 6S-6D transitions in high vacuum, and two versions of vacuum systems were designed to avoid any collision shift, from either cell outgassing or atmospheric helium. Figure 4 exhibits two versions of the vacuum systems that serve as the Cs #2 cell in Fig. 1. In Fig. 4(a), namely, Cs #2-1, a Cs ampule was put into a CF three-way cross chamber labeled "Cs atoms." All parts in the vacuum system were pumped down to 10^{-7} Torr by a mechanical-turbo pumping station. After two weeks of baking, the heat was removed

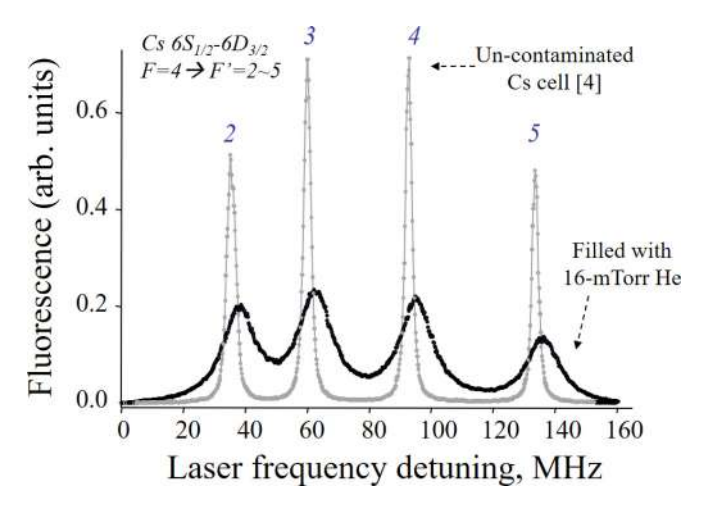


FIG. 3. Influence of helium collision on cesium $6S_{1/2}(F=4) \rightarrow 6D_{3/2}(F'=2-5)$ hyperfine transitions, showing the importance of keeping away the helium contamination from atmosphere [4] (see Table I).

and the gate valve was closed. The chamber was disconnected from the pumping station and was shaken up and down, by which the pigtail of the ampule in Fig. 4 was smashed. The vacuum gauge was removed beforehand to avoid cesium contamination. After the destruction of the ampule was ensured from one viewport (VP*), the all-metal valve was opened to drive the cesium atoms into the condensation region, which is the coldest place in the chamber. To transport Cs atoms from the place of Cs atoms to the condensation region in Fig. 4, we applied a temperature distribution as marked in Fig. 4(a). The highest temperature (100 °C) was applied to the Pyrex windows of the laser input and output and the Pyrex window attached to the PMT to avoid any Cs atom condensation on those windows and to create a cesium-atom condensation region. Figure 5 demonstrated how we found the best pumping rate to avoid the background-gas-Cs collision shift while optimizing the SNR at a condensation-region temperature of 70 °C. The knobs of gate valves in Fig. 5 were rotatable, and the turns of rotation on the transverse axis were considered

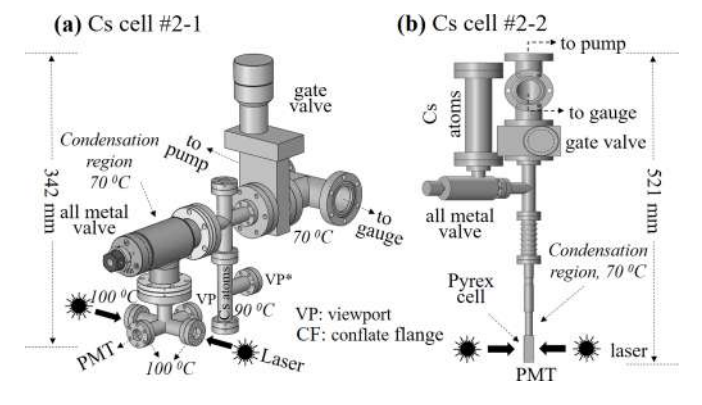


FIG. 4. (a) Cell #2-1 vacuum chamber made of stainless steel and (b) cell #2-2 vacuum chamber where a Pyrex cell is attached. The sizes in each figure are all proportional to real dimensions, whereas the scales are different. Three pairs of Helmholtz coils are not exhibited here [see Fig. 6(b)].

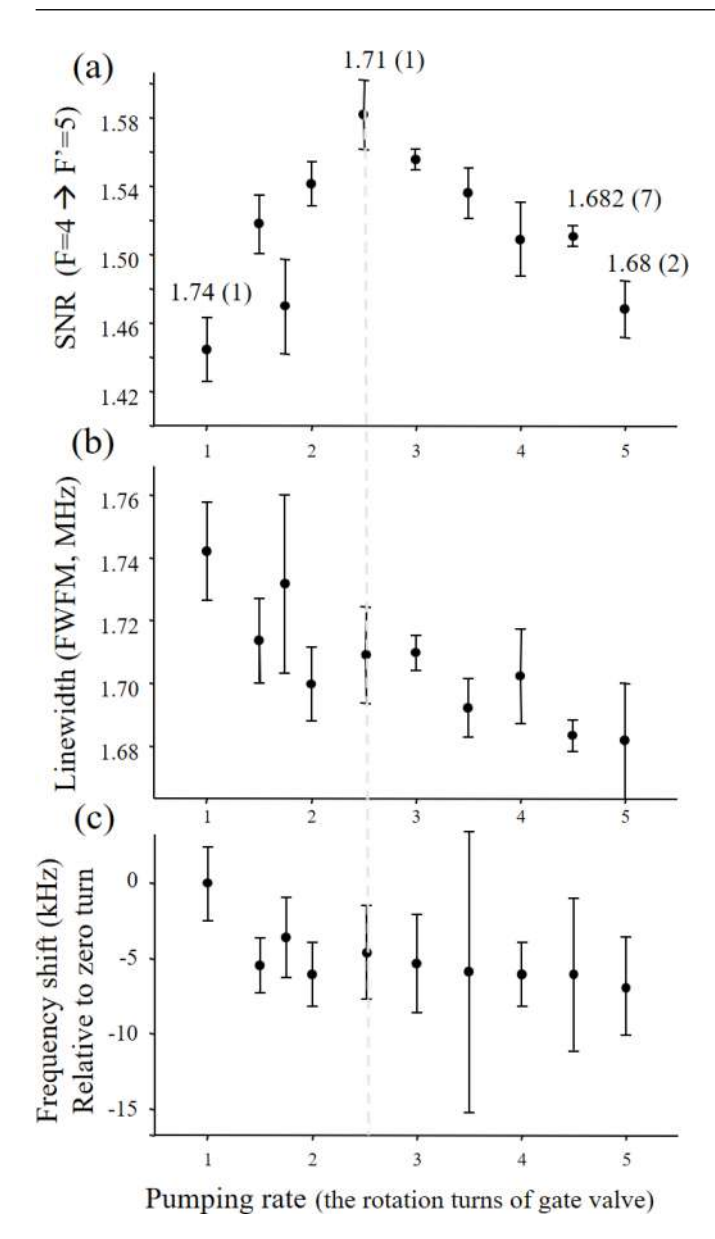


FIG. 5. Choosing a suitable pumping rate to avoid background-gas collisions and to maintain a sufficient SNR, by Cs cell #2-1. (a) SNR versus pumping rate. Some associated numbers are the corresponding linewidths (in megahertz). (b) and (c) Corresponding linewidths and frequency shifts relative to a zero pumping rate. The condensation-region temperature is 70 °C. The gray dashed line separates two regimes of different slopes (see the text for details).

proportional to the pumping rate. Each data point in Fig. 5 was taken after thermal equilibrium. The thermal equilibrium was inspected by a Cs D_2 -line stabilized laser to monitor the atom density. The background gas, like some wall outgassing gases that were lighter than the Cs atom, was believed to dominate the collision broadening from 0 to 2.5 turns since the SNR increases [Fig. 5(a)] with decreasing linewidth [Fig. 5(b)] as the pumping rate is increased. After 2.5 turns, the SNR decreases with increasing pumping rate since the cesium atom number decreases. The gray dashed line separates Fig. 5 into two different regimes regarding different collision partners, that is, the background-gas collision and the Cs-Cs collision.

After 3.5 turns of knob rotation and within our measurement uncertainty, no obvious change for either linewidth or frequency is perceived, judging from Figs. 5(b) and 5(c). This implies that the pumping rate has surpassed the collision rate so that the effective Cs-Cs collision shift is ignorable in determining the transition frequencies. Hence, before the frequency measurements in high vacuum were performed, it was always ensured that the $F = 4 \rightarrow F' = 5$ transition had a linewidth (FWHM) of 1.68 MHz, no matter which cesium cell in Fig. 4 was used, as long as the laser beam size was not changed. Unfortunately, a worldwide-reported earthquake at 7.1 Richter magnitude [18] violently shook the optical table and damaged the vacuum condition. Hence, a second-version vacuum system shown in Fig. 4(b) (Cs #2-2) was developed. The Pyrex glass cell in Fig. 4(b) was designed to be long enough to reach the inside the Helmholtz coils (not shown in Fig. 4), through which the optical table decoupled with the vacuum system. Note that three pairs of Helmholtz coils were always installed for both designs. The procedures for preparing the cesium atoms, including the atoms' transportation and the temperature gradient, are very similar to those in Fig. 4(a). The comparisons of the experimental results under two different vacuum systems will be discussed in Sec. IIF. Those two versions of vacuum systems offer a good chance of testing the frequency reproducibility, which is an important issue if the Cs $6S_{1/2} \rightarrow 6D_{3/2}$ hyperfine transition is considered as a candidate for a clock transition in the 885-nm-wavelength regime. The conclusion from Fig. 5 is that no collision shift was perceived within our measurement uncertainties, as the pumping rate was larger than the 3.5-turn gate-valve rotation. We also inspected the Cs-Cs collision in a sealed cell by changing the temperature of the condensation region in Cs cell #2-1. See Appendix B for the results.

C. Compensating Zeeman shift directly from the spectral linewidth measurements

There are two conventional approaches to suppress the undesired Zeeman shift: One active approach is to build up three pairs of Helmholtz coils together with a high-precision Gauss meter for a *B*-field (magnetic field) calibration; another passive way is to shield away the B field via a high- μ -metal housing. We found that Helmholtz coils could not guarantee zero magnetic field inside the cesium container, either the metal chamber (Cs cell #2-1) or the glass cell (Cs cell #2-2). In particular, the cesium containers need to be heated up such that the heaters yield different residual magnetic fields depending on the temperatures required and on the different materials of the containers. The drawback of the latter approach is that we never know how sophisticated housing is sufficient under a request of limited space, not to mention that heating cells to achieve high temperatures easily degrades the value of μ (permeability). In this section we demonstrate an alternative approach for compensating for the influence of the residual magnetic field directly from the information of the atoms inside the containers. The OLCS in Fig. 1 was used to monitor the subtle change of Zeeman broadening, by which we could find the near-zero-magnetic-field linewidth, as demonstrated in Fig. 6(a). When we adjusted the x component of the B field via the Helmholtz coils whose x direction

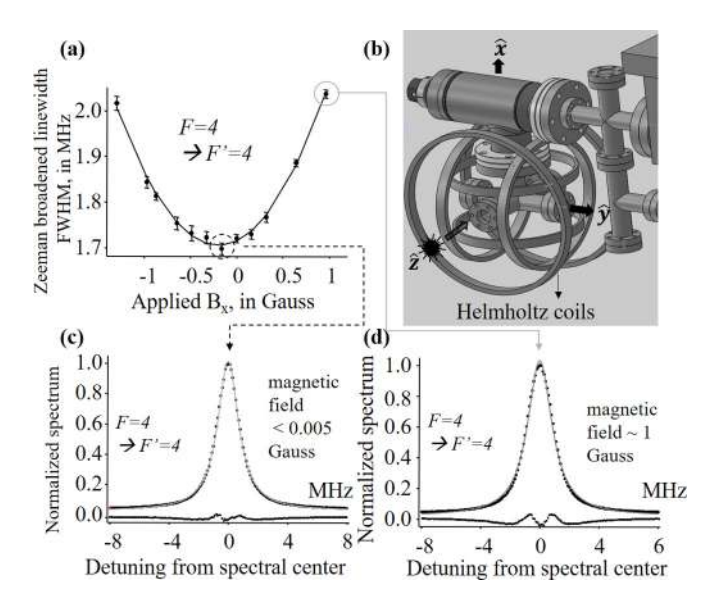


FIG. 6. (a) Zeeman broadening vs applied magnetic field, measured via the setup in (b) and taking B_x as an example. (b) Helmholtz coils for implementing for both Cs cells shown in Fig. 4; here we use Fig. 4(a) as an example; \hat{z} is the beam-propagating direction. (c) Typical near-zero-B spectrum and the fitting residual of the data. (d) Zeeman-broadened line shape, fitted by a Lorentzian transit-time function.

is defined in Fig. 6(b), a weak magnetic field was tuned to obtain the data in Fig. 6(a). The same procedure of determining the narrowest linewidth was also applied to the other two directions. The supporting frame of the coils in Fig. 6(b) was made from a 3D printer. Figure 6(c) is sketched from the same spectrum of the smallest-linewidth data indicated by a dashed circle in Fig. 6(a), from which the spectrum can be perfectly fitted by a Lorentzian transit-time function (gray curve) with 25-time-smaller fitting residual (± 0.02) than the signal height. The same function can even be used to fit the line shape of the largest Zeeman-broadened data in Fig. 6(a), indicated by a closed gray circle, with merely twice larger fitting residual, as illustrated in Fig. 6(d). This certifies that the Zeeman splits are small enough for a Lorentzian transit-time fitting. The relation between the Zeeman-broadened linewidth $\Gamma(B)$ and the magnetic field B was experimentally found to be a quadratic function, as is illustrated by the black curve in Fig. 6(a), which can be theoretically proved in Appendix C. This approach of compensating for the surrounding B field was first demonstrated by Chu et al. in searching for the zero-B-field rubidium optical clock frequency [3]. In this section we show the detailed calculations (Appendix C) with a demonstration based on cesium atoms. With this approach, the residual magnetic field (RMF) could be reduced to around 1 mG, limited by the sensitivity of our Gauss meter on hand [19]. Even if we conservatively estimate a 5-mG RMF and suppose the direction of the RMF is right along the z direction, the residual Zeeman shift is merely 120 Hz according to the slope of the black data in Fig. 7. The three stars in Fig. 7 further point out the data of narrowest linewidths corresponding to the three directions in space, among which one star colored blue is just the same data of the narrowest linewidth data in

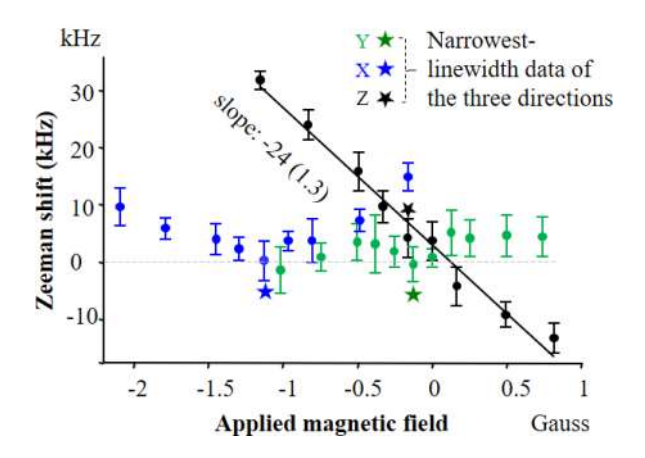


FIG. 7. Zeeman shift measurements. The data marked with colored stars have the narrowest linewidth corresponding to each direction defined in Fig. 6(b): blue star, x direction; green star, y direction; and black star, z direction.

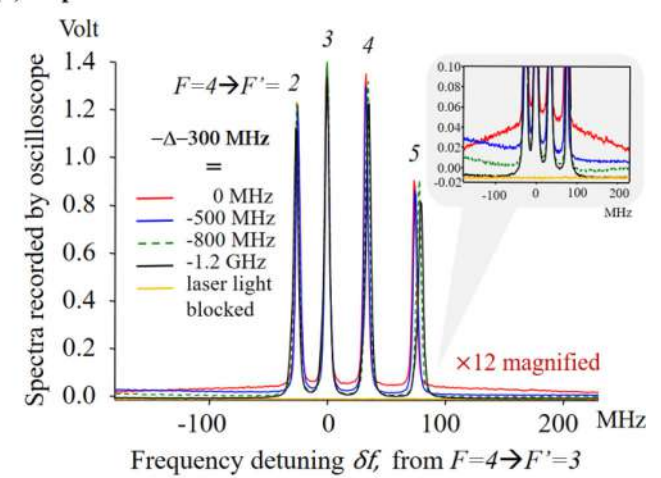
Fig. 6(a). The positions of the three stars in Fig. 7 imply that the original magnetic field, right above the optical table, is around 1.15 G in the X direction and around 0.20 G in the Y and Z directions, where the Z direction is the laser beam propagation direction. The Zeeman shifts (slope) are almost the same for both Cs cells #2-1 and Cs #2-2 displayed in Fig. 4, except for different amounts of applied B field (current) to search for the narrowest linewidth.

D. Removing the residual Doppler background by the crossover spectra

High-resolution two-photon spectroscopy normally attaches a small asymmetric pedestal around each main line [20,21], which is referred to as residual Doppler background in this paper. The asymmetric shape of the pedestal comes from the line shape pulling by the nearby pedestals as exhibited in the gray inset of Fig. 6(a), red curve. Such a Doppler background results from the two-photon self-excitation with a certain atom velocity and can only be avoided by selection rules like the *S-S* transition together with circular light polarization [13]. Therefore, both in this paper and in the rubidium *S-D* clock transition, RDB is an inevitable error source in the issue of the clock. We here report a scheme to remove the residual Doppler background by the two-photon crossover spectrum [14], no matter what the selection rules are.

To experimentally prove that the two-photon crossover spectrum could eliminate the RDB, two flip-flop mirrors in Fig. 1 were flipped down and the modulation on AOM1 was turned off while the +1 order of the double-pass AOM1 and the -1 order of the single-pass AOM2 were employed. Consequently, as illustrated in Fig. 1, the beam 1 frequency f_{beam1} became $f_{\text{PS}} + 200$ MHz and the counterpropagating beam 2 frequency f_{beam2} equals $f_{\text{PS}} - 100$ MHz $-\Delta$, where f_{PS} stands for the frequency of ECDL #1 and Δ stands for the offset frequency. By adjusting the offset frequency Δ between two lasers, the frequency difference between the two beams $f_{\text{beam2}} - f_{\text{beam1}}$ could be adjusted from 0 MHz to -1.2 GHz. In other words, $f_{\text{beam2}} - f_{\text{beam1}}$ always equals $-\Delta - 300$ MHz, in which Δ equals $f_{\text{OL}} - f_{\text{PS}}$, where f_{OL}

(a) Experimental results



(b) Theoretical simulation

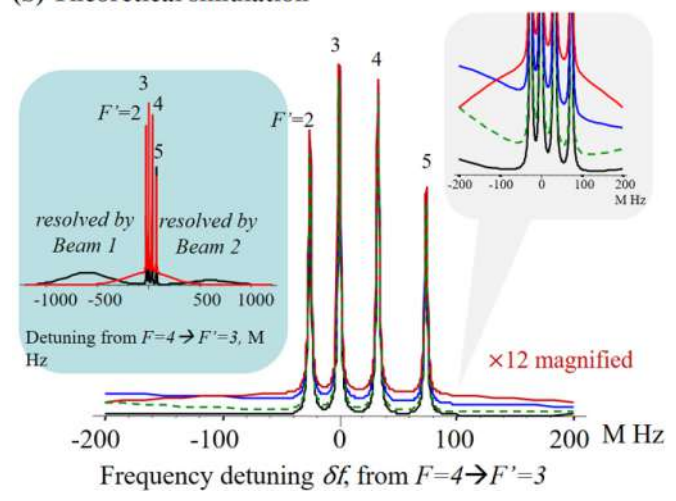


FIG. 8. (a) Results of experimental demonstration removing the Doppler background. (b) Results of theoretical simulation (see te text for details). Here f_m is the frequency of the master laser and Δ is the offset frequency, equal to $f_{\rm slave} - f_{\rm master}$.

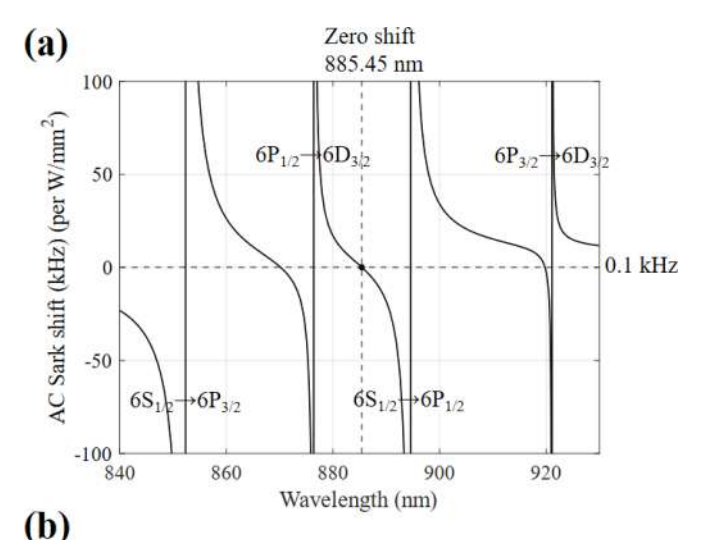
stands for the frequency of ECDL #2. The experimental results of Fig. 8(a) show that, as $f_{\text{beam2}} - f_{\text{beam1}} = -1.2 \text{ GHz}$ (black curve), the residual Doppler background could be suppressed to be one order of magnitude smaller than the situation where $f_{\text{beam2}} - f_{\text{beam1}} = 0$ (red curve). In Fig. 8(a) the prestabilized laser was freely running during scanning of the laser frequency by one piezoelectric transducer, which is the reason why the hyperfine components could not all overlap with each other between several scans, despite the offset lock between the two lasers always being performed in each scan. The spectra in Fig. 8 are referred to as a two-photon crossover [14] because they only appear when the mean frequency of two beams $(f_{\text{beam1}} + f_{\text{beam2}})/2$ is resonant with a certain transition. Figure 8(b) is our simulation that illustrates the physics of Fig. 8(a), in which the 50-mW power of beam 1 in Fig. 1 and the 30-mW power of beam 2 are employed; a 200-MHz Doppler broadening and 1.7-MHz Lorentzian linewidth are employed in the simulation. The light blue inset on the left side of Fig. 8(b) compares two situations from the perspective of a five-time-wider frequency scanning range than in Fig. 8(a). The red curve is sketched under the situation of $f_{\rm beam2} - f_{\rm beam1} = 0$, while the black curve is for $f_{\rm beam2} - f_{\rm beam1} = -1.2$ GHz, which shows that the two-photon crossover spectra could be located upon a flat background as long as $f_{\rm beam1} - f_{\rm beam2}$ is large enough, by which we remove the RDB. As 1.2 GHz is around 4.6 times the Doppler width (0.26 GHz), the RDB of the black curve in Fig. 8(a) is 4.8×10^{-5} of the signal height, which corresponds to a subhertz frequency pulling resulting from the high-speed atoms (Doppler wing). The red curve in Fig. 8(a) is resolved by the two counterpropagating beams of the same frequencies, where the line pulling by nearby RDB is estimated as 160 Hz (see the curve fitting in Appendix A).

E. Naturally small ac Stark shift

The ac Stark shift in an atomic two-photon transition results from summing the transition amplitudes over all transition pathways, which is influenced by the intermediate states [21]. In other words, the atomic structure naturally determines this error source (ac Stark shift), which is inevitable if only a single-frequency laser is used. This is the thorniest term in the uncertainty budget of a two-photon transition-based optical clock, in general. To get rid of this error source, the simplest solution is to find a suitable transition that naturally balances the redshift from the blueshift among all transition pathways. Luckily, we experimentally found that the cesium $6S_{1/2}$ - $6D_{3/2}$ hyperfine transitions yield an impressively small ac Stark shift. The theoretical calculation in Fig. 9(a) shows only a 0.1 kHz/(W mm²) ac Stark shift at 885.40-nm wavelength. This is reasonable since the magic wavelength (zero shift) is predicted at 885.45 nm. Two transitions having the smallest ac Stark shifts in our experiments are picked up to be presented in Fig. 9(b). The measurement uncertainties of Fig. 9(b) overlap with each other, which implies that the true ac Stark shifts of those two cesium transitions might be even smaller than the fitted opposite-sign slopes in Fig. 9(b). That means our laser intensity is not large enough to reveal the ac Stark shift of the two transitions. To compare Cs ac Stark shifts to that of the Rb clock 5S-5D transition measured under the same circumstances [3], we intentionally designed a similar beam waist and performed the measurements with the same power meter and the same comb laser system as what was installed in Ref. [3]. Figure 9(b) shows that the ac Stark shifts of cesium $6S_{1/2}$ $(F = 4) \rightarrow 6D_{3/2}$ (F' = 4, 5) transitions (solid lines) are one order of magnitude smaller than that of the Rb 5S-5D clock transition (dashed line). This is mainly because the frequency of the fundamental radiation (885 nm) is red detuned concerning the Cs D2 transition (852 nm) and the $6P_{1/2} \rightarrow 6D_{3/2}$ (874 nm) transition, while is blue detuned to the D1 transition (892 nm) and the $6P_{3/2} \rightarrow 6D_{3/2}$ (917 nm) transition, as indicated in Fig. 9(a).

F. Frequency reproducibility, traceability, and uncertainty budget

Studying all possible frequency shifts to give an uncertainty budget is essential for deciding whether those atomic transitions are qualified to be a reliable frequency reference.



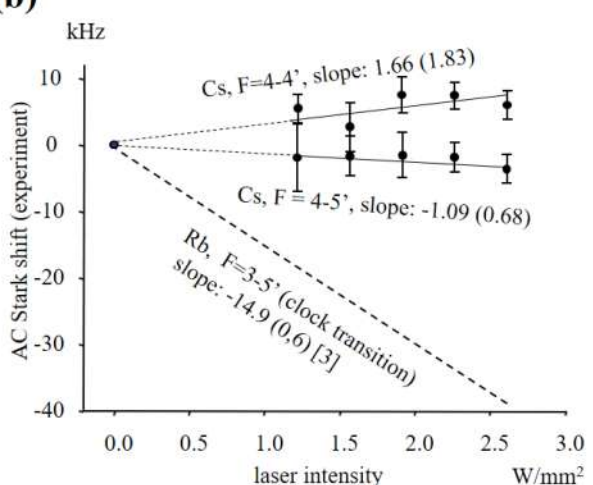


FIG. 9. Plot of the ac Stark shift. (a) Simulation shows that the zero-shift wavelength is at 885.45 nm, and the 885.40-nm two-photon transition wavelength yields a shift of 0.1 kHz/(W/mm²). (b) Experimental results, one of which yields a slope approximately 14 times smaller than that of the Rb-clock transition (short dashed line).

Figure 10 shows the frequency reproducibility and frequency traceability [22] of our measurements. Each data point in Fig. 10 was obtained after the linewidth of the $F=4 \rightarrow F'=5$ transition was confirmed to be 1.68 MHz, as mentioned in Sec. II B. More specifically, the two data colored in black in Fig. 10 are the determined frequencies of $F=4 \rightarrow F'=5$ transitions, and they are conventionally called absolute frequencies except that the blackbody radiation shift is too small

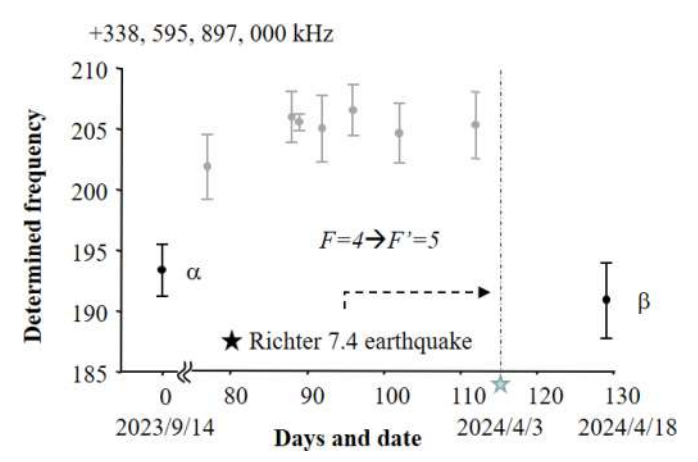


FIG. 10. Traceability and reproducibility tests. Gray data points were obtained from the same commercial Cs cell; α data point was obtained using Cs cell #2-1 and β data point was obtained using Cs cell #2-2 (see Fig. 4 and Table II for details).

to be aware of in this experiment. The frequencies determined in this paper are then referred to as transition frequencies instead. The two data were measured with sufficiently separated days and were under very different circumstances, as compared in Table II. The earlier-day data α data point in Fig. 10 was obtained based on the vacuum structure of Fig. 4(a) (Cs cell #2-1), whereas the latter data point β was obtained via the design of Fig. 4(b) (Cs cell #2-2). The main differences are (i) Cs cell #2-2 was under full pumping (a fully opened gate valve) and thus the SNR is around one-sixth smaller than that of the data α ; (ii) the frequency of the comb laser used in the earlier measurement referred to one Rb microwave clock which was calibrated by a cesium atomic beam clock, together with a hydrogen clock, before experiment [23], whereas the frequency of the comb laser in the latter measurement referred directly to one cesium atomic beam clock [24]; and (iii) the β data point was completed amid perceptible aftershocks [25] that led to a larger error bar, whereas the earlier α data point was obtained under normal laboratory conditions. The frequency comparison between α and β gives a frequency reproducibility of 2.6 kHz. When the high-vacuum cell (Cs #2 in Fig. 1) was replaced by a commercial glass cell, the measurement results (seven gray data in Fig. 10) present an obvious frequency discrepancy from that of α and β data. Since all the linewidths of the gray data are more broadened by more than 400 kHz than those of α and β data, some background-gas-collision broadening was suspected to be involved in the gray data owing to our empirical conjecture

TABLE II. Comparison of circumstances obtaining the α and β data indicated in Fig. 10.

Data	Date	Vacuum cell (see Fig. 4)	Pumping rate (see Fig. 5)	
α	14 Sep 2023	Cs cell #2-1	Gate valve four turns	
β	18 Apr 2024	Cs cell #2-2	Gate valve fully open	
	Laboratory conditions	Frequency reference for comb laser		
α	Normal	Rb rf clock [23], frequency calibrated by a hydrogen clock and a cesium atomic beam clock		
β	Aftershocks, NE monsoon	Directly via cesium atomic beam clock [24]		

TABLE III. Uncertainty budget ($F = 4 \rightarrow F' = 5$, cell #2-2).

Error source	Uncertainty (kHz)	Details
Statistical error	±3	Sec. II F
Second-order Doppler	± 0.28	
Line pulling	± 0.16	Appendix A
ac Stark shift	± 0.15	Sec. II E
Zeeman shift	± 0.12	Sec. II C
Cs atomic beam clock	± 0.05	[24]
Collision shift	Unperceived	Sec. II B

from the cesium 6S-8S experiments [4]. On the other hand, all the gray data confirmed that our experimental setup could provide a frequency traceability of ± 1.5 kHz, though they lost the accuracy. Since we always heated this commercial cell up to more than 80 °C, it could speed up the helium diffusion from the atmosphere. The blueshift of the gray data in Fig. 10 implies that a mixture of helium [26] and wall outgassing gas play an important role in the contamination of the cesium cell. Table III exhibits the uncertainty budget in determining accurately the frequency of the $F = 4 \rightarrow F' = 5$ transition, as an example for all other hyperfine transitions. The line pulling by the residual Doppler background of the nearby spectrum was apparent from the different fitting functions mentioned in Appendix A. The ac Stark shift measured in Sec. IIE is so small that higher laser power is needed to further narrow down this uncertainty. As for the Zeeman-shift error, please refer to Sec. II C and Fig. 7 for this uncertainty budget. The collision-shift error was not perceived as the pumping rate is high enough, which was mentioned in Sec. II B.

The statistical error dominates all uncertainty sources. Moreover, Fig. 10 shows that the error bar of β data is larger than the error bar of α data. All hyperfine transitions have the same error-bar-enlargement problem after the Richter 7.4 earthquake; two transitions in Table IV are examples. We suspected that some unlisted error sources like the perceptible aftershocks [25] and the shaking of the building caused by the northeast monsoon (October to April) might contribute to the statistical error since our laboratory is on the fourth floor of a ten-floor building and our building is located on a hill which is only 21 km away from the Taiwan Straits. More repeated measurements did not help reduce the leading uncertainty (statistical error) listed in Table III. The aforementioned low-frequency noise could be perceived by comparing the Allan deviations measured under normal laboratory condition and under β conditions described in Table II, as shown in

TABLE IV. Transition frequency, measured in high vacuum. Column 1 lists the same measurement conditions as the α and β data as in Fig. 10, referring to Sec. II F.

Conditions	Transition	Transition frequency (kHz)
α	$F = 4 \rightarrow F = 5'$	$338, 595, 897, 193.4 \pm 2.1$
α	$F = 4 \rightarrow F = 4'$	$338, 595, 856, 369.0 \pm 2.6$
β	$F = 4 \rightarrow F = 5'$	$338, 595, 897, 190.8 \pm 6.4$
β	$F = 4 \rightarrow F = 4'$	$338, 595, 856, 370.2 \pm 4.2$
β	$F = 3 \rightarrow F = 5'$	$338,600,493,509.9 \pm 3.6$

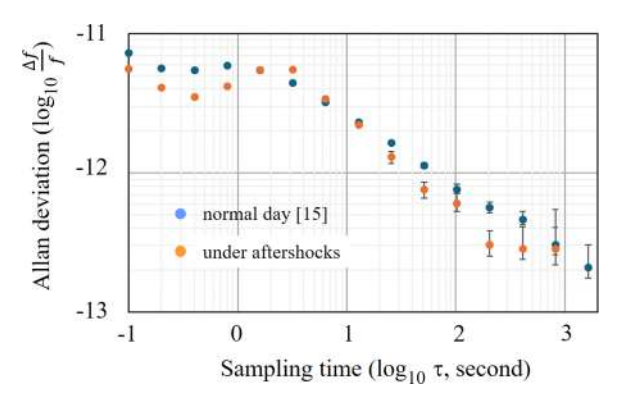


FIG. 11. Comparison between two two-sample Allan deviations obtained on a normal day and under the β conditions described in Table II.

Fig. 11. All the Allan deviations were obtained by beating the frequency of a Cs-stabilized 885.4-nm diode laser against the same comb laser. From Fig. 11 some abnormal Allan deviation in orange color at the sampling time from 0.1 s to 1.6 s is perceived.

III. TRANSITION FREQUENCIES, HYPERFINE CONSTANTS, AND HYPERFINE LINEWIDTHS

Table IV summarizes the transition frequencies mentioned in this paper, which are one order of magnitude better precision than our previous work [16], through which the present values of the eigenfrequencies have been updated. In Table IV the measured frequencies under α and β conditions are also compared. The hyperfine constants are updated in Table V and are compared with previous works [16,27]. The previous data in Table V were all obtained based on commercial Cs glass cells, which is the main reason for the difference from this work. The hyperfine structure is influenced by the charge distribution of the atomic nucleus [28], and the coupling between the electron and the fields caused by the nuclear charge distribution can be expressed by treating the multipole expansions as the perturbation term H' in its Hamiltonian

$$H'_{\text{hyperfine}} = H_{\text{magnetic dipole}} + H_{\text{electric quadrupole}}$$
 (1)

or in terms of the difference of the eigenfrequencies

$$\frac{\Delta E}{h} = \Delta f_{\text{hyperfine}}$$

$$= A(\mathbf{I} \cdot \mathbf{J}) + B \frac{3(\mathbf{I} \cdot \mathbf{J})^2 + \frac{3}{2}(\mathbf{I} \cdot \mathbf{J}) - I(I+1)J(J+1)}{2I(2I-1)J(2J-1)}$$

$$+ \cdots . \tag{2}$$

TABLE V. Hyperfine constants A and B (in megahertz).

Hyperfine constant	Cell #2-2 ^a	Cell #2-1a	Ref. [16] ^b	Ref. [27] ^b
A	16.337(1)	16.337(1)	16.338(3)	16.34
В	-0.058(18)	-0.042(20)	-0.136 (24)	-0.1(2)
C			2.536(8)	

^aVia a high-vacuum cell.

^bVia a commercial glass cell.

TABLE VI. Linewidth (FWHM) of each hyperfine component (in megahertz).

Lower level	Upper level	High vacuuma	Glass cellb
$6S_{1/2}, F = 4$	$6D_{3/2}, F = 5$	1.40(2)	1.680(8)
,	$6D_{3/2}, F = 4$	1.36(2)	1.760(6)
	$6D_{3/2}, F = 3$	1.37(2)	2.128(6)
	$6D_{3/2}, F=2$	1.46(1)	2.536(8)
$6S_{1/2}, F = 3$	$6D_{3/2}, F = 5$	1.38(10)	2.464(6)
,	$6D_{3/2}, F = 4$	1.36(2)	2.438(12)
	$6D_{3/2}, F = 3$	1.38(2)	1.920(22)
	$6D_{3/2}, F = 2$	1.49(1)	1.672(64)

^aCs cell #2-2, with the Lorentzian-part linewidth in the Lorentzian transit-time fitting at a 0.42(2)-mm beam waist.

Together with the addition theory of angular moment

$$\mathbf{I} \cdot \mathbf{J} = \frac{F(F+1) - J(J+1) - I(I+1)}{2},$$
 (3)

one can derive the hyperfine constants A and B from the hyperfine intervals $\Delta f_{\text{hyperfine}}$ at different F and F' quantum numbers [16,27]. The following three hyperfine intervals were obtained from Cs cell #2-1 due to better SNR, as mentioned previously:

$$\Delta f_{\text{hyperfine}}(F' = 2 \rightarrow 3) = 24522.7 \times 2 \pm 6.1 \text{ kHz}, \quad (4)$$

$$\Delta f_{\text{hyperfine}}(F' = 3 \rightarrow 4) = 32686.1 \times 2 \pm 4.3 \text{ kHz}, \quad (5)$$

$$\Delta f_{\text{hyperfine}}(F' = 4 \rightarrow 5) = 40\,820.6 \times 2 \pm 5.4 \text{ kHz}.$$
 (6)

The frequency of the centroid can be deduced from the above spectral information as 338 597 865 202.2 (37) kHz.

It is worth of noting that there are two guidelines for selfinspecting the frequency accuracy in Tables IV and VI. One is to check if twice the frequency difference between $F = 4 \rightarrow$ F' = 5 and $F = 3 \rightarrow F' = 5$ transitions [9 192 638.2(13.3) kHz] is consistent with the microwave clock frequency (9 192 631 778.0 Hz). The other is to check the linewidth for the spectrum of interest. The measurement of the spectral linewidth is very important in monitoring the broadening caused by residual magnetic field, atom collision, laser frequency jitter, transit-time broadening, and so on. Therefore, keeping in mind that the up-to-date narrowest linewidth is essential for the self-inspection of the accuracy of the transition frequency, as the linewidth broadening-frequency shift relation has been proved to be a good guidance for finding the accurate two-photon transition frequency previously [3,4], Table VI gives all the Lorentzian-part linewidths for the guideline of accurately searching the transition frequencies in spite of different transit-time broadenings in different optical layouts. In our case, the beam waist at the center of the cesium cell #2 is around 0.42 mm. In Table VI the 1.4-MHz linewidth is consistent with the theoretical calculation of the natural linewidth [29]. Column 4 in Table VI is our previous measurement [16], from which a slightly contaminated glass cell used in the previous experiment is suspected, owing to a broader linewidth.

IV. CONCLUSION

To summarize, a two-photon transition in alkali-metal atoms could be a reliable optical-frequency-standard transition as we successfully removed or depressed several main systematic errors. We demonstrated that high-precision linewidth measurement is a reliable approach to confirm the accuracy of the atomic transition frequency. A cavity-enhanced spectrometer might further improve the frequency accuracy since it could reduce the error from wavefront curvature distortion [20], though this error is not the main concern in this work. The experimental results here not only provide the updated eigenvalues for the theory of cesium atomic parity nonconservation but also show the promise of establishing more two-photon transition-based optical frequency standards in high vacuum, as demonstrated in Ref. [3].

ACKNOWLEDGMENTS

We are grateful to Professor Li-Bang Wang for very helpful discussions and for lending us a Gauss meter for such a long term; Dr. Ming-Shien Chang kindly provided us a pumping station for high vacuum. This research was funded by the National Science and Technology Council, Taiwan (Grant No. 114-2112-M-008-025).

DATA AVAILABILITY

The data are available from the authors upon reasonable request.

APPENDIX A: FITTING FIG. 2 SPECTRA WITH DIFFERENT FITTING FUNCTIONS

In the following we use two different fitting functions to compare the fitting residuals of the spectra in Fig. 2. Figure 12(a) is the residual of fitting a Lorentzian-Gaussian background function, in which the Gaussian linewidth (HWHM) is set to 263.89 MHz, that is, the fitting function L is

$$L(f) = y_0 + \sum_{n=1}^{4} \left(\frac{a_n}{1 + \left(\frac{f - f_n}{\Gamma_n}\right)^2} + b_n e^{-[(f - f_n)/263.89]^2} \right),$$
(A1)

where f_n is the resonant frequency of the nth hyperfine transition and Γ_n is the corresponding linewidth (HWHM). Figure 12(b) shows the residual from the fitting of a Lorentzian transit-time function [17], which yields the same residual as that exhibited in Fig. 2. The fitting function is expressed as

$$L(f) = y_0 + \sum_{n=1}^{4} \left(\int_{-\infty}^{\infty} \frac{c_n \, \Gamma_n}{(\Omega - \Delta_n)^2 + \left(\frac{\Gamma_n}{2}\right)^2} e^{-\left[(|\Omega - \Delta_n|)/\delta\right]^2} d\Omega \right), \tag{A2}$$

where $\Delta_n \equiv f - f_n$ and $\delta \ln 2$ is the width (HWHM) of the transit-time broadening. Since the former case can efficiently eliminate the background, we believe that the background

^bLorentzian fitting, with a beam waist of 1.3(3) mm via Cs #3 in [16], corresponding to a transit-time broadening of approximately 0.1 MHz.

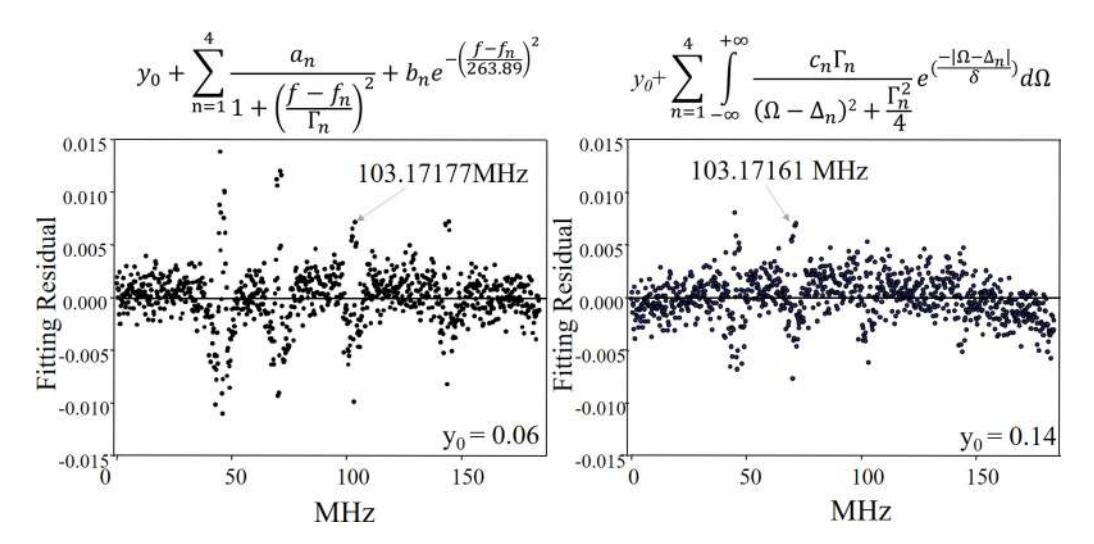


FIG. 12. Comparison of the fitting residuals obtained using two different fitting functions. The same data as shown in Fig. 2, for the $F = 4 \rightarrow F' = 2, 3, 4$ transitions, are fitted.

of the fitting residual in Fig. 2 results from the residual Doppler background. The reason we chose the Lorentzian transit-time fitting function to determine the transition frequency is twofold. One is that the fitted linewidths of both the Lorentzian part and the transit-time part agree very well with the theoretical calculations for the natural linewidth (approximately 1.3 MHz) [29] and the transit-time broadening (approximately 300 kHz) [17]. Moreover, we have observed the change of the fitted linewidth in the transit-time part as the beam size was varied, while the Lorentzian-part linewidth remained unchanged. The other reason is that Lorentzian transit-time fitting yields the smallest residual among all other fitting functions, such as Voigt and Lorentzian. However, the Lorentzian transit-time function is not able to fit the residual Doppler background very well. More fitting parameters might work, but could not give reasonable linewidths, including the transit-time broadening. The determined frequency of the $F = 4 \rightarrow F' = 4$ transition for two different fitting functions differs for 160 Hz, which is the reason we conservatively quote the error of the line-pulling effect (by the residual Doppler background) to be ± 0.16 kHz in Table III, since we did not know which fitting function was more correct. This is the reason we proposed an approach in Sec. II D to depress the aforementioned residual Doppler background, which eliminated the concern about fitting the Doppler background.

APPENDIX B: PRESSURE SHIFT IN A SEALED HIGH-VACUUM CELL

Many applications need a sealed cell for convenience. In the following we investigate the pressure shift under a sealed cell, though the transition frequency in this paper was not determined by any sealed cell. The collision rate was varied by changing the condensation-region temperature in Cs cell #2-2. After finding the narrowest-linewidth spectrum from Fig. 6, the gate valve of the Cs cell #2-2 in Fig. 4 was then closed; afterward, the vacuum chamber was disconnected from the pumping station by closing the gate valve. Each data point in Fig. 13 was taken after the thermal equilibrium had been reached. The thermal equilibrium was confirmed

from a steady absorption of an 852-nm laser light whose frequency was prestabilized to the cesium D_2 line. During the time interval between two successive condensation-region temperatures, the vacuum chamber was reconnected to the pumping station again until the vacuum was below 10^{-5} Torr, to ensure that no outgassing from the chamber was involved in the next data acquisition. This step is vital for Fig. 13, since we always found the linewidth being broadened as the cell was kept sealed for several days. The conclusion of this inspection is that a glass-cell-based clock with no outgassing problem would still be a reliable optical frequency reference since the collision shift from the glass wall or Cs-Cs collision is not obvious in Fig. 13, as long as the temperature in Fig. 13 is below 70 °C.

APPENDIX C: USING SPECTRAL LINEWIDTH TO DETECT RESIDUAL MAGNETIC FIELD

Let the Zeeman-broadened line shape $L(B, \Delta \nu)$ in Fig. 6 be expressed simply as a superposition of all Zeeman sublevels, where B stands for the magnetic field applied to those atoms that interact with light and $\Delta \nu$ is the laser frequency detuning from the resonant frequency at zero B field. Let the F=4

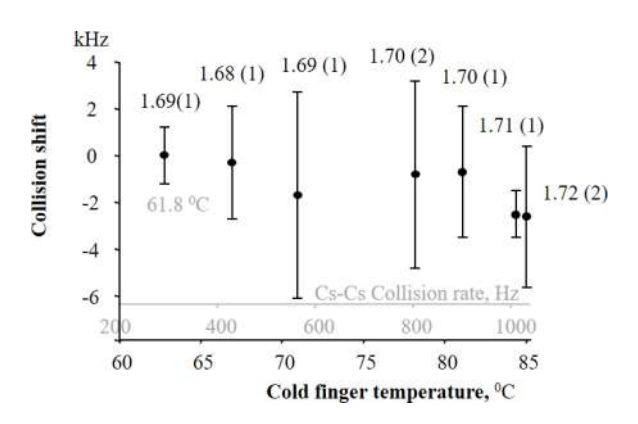


FIG. 13. Collision shifts in a sealed cell. The number associated with each data point is its linewidth (in megahertz).

F' = 4 transition be chosen as an example for the line-shape analysis

$$L(B, \Delta \nu) = \sum_{m=-4}^{4} \frac{A_{0m} E_0^2}{\left(\frac{\Delta \nu + m\delta B}{\Gamma_0}\right)^2 + 1} + \sum_{m=-4}^{2} \frac{A_{+m} E_+^2}{\left(\frac{\Delta \nu + (m\delta - \Omega)B}{\Gamma_0}\right)^2 + 1} + \sum_{m=-2}^{4} \frac{A_{-m} E_-^2}{\left(\frac{\Delta \nu + (m\delta + \Omega)B}{\Gamma_0}\right)^2 + 1},$$
 (C1)

where $\delta \equiv \mu_B(g_F - g_{F'})/h$; $\Omega \equiv 2\mu_B g_{F'}/h$, with g_F and $g_{F'}$ the Landé g factors of the lower and upper levels, respectively; μ_B is the Bohr magneton; h is the Planck constant; Γ_0 is the zero-B linewidth (HWHM); A_{0m} , A_{+m} , and A_{-m} are the weak-light absorption coefficients of the Zeeman sublevels induced by the light of linear ($\Delta m =$ 0), left-circular ($\Delta m = +2$), and right-circular polarization $(\Delta m = -2)$, respectively; and E_0^2 , E_+^2 , and E_-^2 denote the corresponding light intensities of linear, right-circular, and left-circular polarization, respectively. For a specific transition, as demonstrated in Fig. 6, the $S_{1/2} F = 4 \rightarrow D_{3/2} F' = 4$ transition, the Landé g factors of the lower and upper levels are 0.24994 (g_F) and 0.15959 $(g_{F'})$, respectively [30,31]. The line-shape comparison between Figs. 6(c) and 6(d) implies that those numerous lines presented in Eq. (C1) are strongly overlapped such that even a single Lorentzian function can still fit the overall line shape well. Therefore, we can approximate Eq. (C1) with one central unchanged line (m = 0) and the two most far-detuned lines, i.e., m = +4 for left-circular polarization and m = -4 for right-circular polarization, expressed as

$$L(B, \Delta \nu) \approx \frac{A_0 E_0^2}{\left(\frac{\Delta \nu}{\Gamma_0}\right)^2 + 1} + \frac{A_+ E_+^2}{\left(\frac{\Delta \nu - \alpha B}{\Gamma_0}\right)^2 + 1} + \frac{A_- E_-^2}{\left(\frac{\Delta \nu + \alpha B}{\Gamma_0}\right)^2 + 1},$$
 (C2)

where $\alpha \equiv \mu_B (2g_F - 4g_F')/h$ and A_0 and A_{\pm} are the corresponding effective absorptions. When the laser detuning $\Delta \nu$ is equal to Γ_0 , the signal height derived from Eq. (C2) will be

$$L(B, \Gamma_0)|_{\Delta \nu = \Gamma_0} = \frac{A_0 E_0^2}{2} + \frac{A_+ E_+^2}{2\left(1 - \frac{\alpha B}{\Gamma_0} + \frac{\alpha^2 B^2}{2\Gamma_0^2}\right)} + \frac{A_- E_-^2}{2\left(1 + \frac{\alpha B}{\Gamma_0} + \frac{\alpha^2 B^2}{2\Gamma_0^2}\right)}.$$
 (C3)

As the condition of the weak magnetic field is assumed, i.e., $\alpha B \ll \Gamma_0$, Eq. (C3) can be approximated using the binomial expansion to the first-order term as

$$L(B, \Gamma_0)|_{\delta\nu=\Gamma_0} = \left(\frac{A_0 E_0^2}{2} + \frac{A E_+^2 + A E_-^2}{2}\right) + \left(\frac{A E_+^2 - A E_-^2}{2}\right) \frac{\alpha B}{\Gamma_0} - \left(\frac{A E_+^2 + A E_-^2}{4}\right) \frac{\alpha^2 B^2}{\Gamma_0^2}.$$
 (C4)

Here we let $A_+ = A_- \equiv A$ as the Clebsch-Gordan coefficients of the corresponding Zeeman sublevels are symmetric to each other. Let $\Delta L(B)$ stand for the different signal magnitudes between the situations of $\Delta \nu = \Gamma_0$ and $\Delta \nu = \Gamma(B)$. Then

$$\Delta L(B) \equiv L(B, \Gamma_0) - L(B, \Gamma) = L(B, \Gamma_0) - \frac{1}{2}L(B, 0),$$
(C5)

where 1/2L(B, 0) can be deduced from Eq. (C2) as

$$\frac{1}{2}L(B,0) \approx \frac{A_0 E_0^2}{2} + \frac{A(E_+^2 + E_-^2)}{2} \left(1 - \frac{\alpha^2 B^2}{\Gamma_0^2}\right) r. \quad (C6)$$

Combining Eqs. (C4)–(C6), one can derive explicitly a quadratic function $\Delta L(B)$ as

$$\Delta L = \frac{A(E_{+}^{2} - E_{-}^{2})}{2} \frac{\alpha}{\Gamma_{0}} B + \frac{A(E_{+}^{2} + E_{-}^{2})}{4} \frac{\alpha^{2}}{\Gamma_{0}^{2}} B^{2}, \quad (C7)$$

$$\Gamma = \Gamma_{0} + \frac{\Delta L}{\tan \theta}, \quad (C8)$$

where $\tan \theta \approx \frac{dL(B,\Delta\nu)}{d\Delta\nu}|_{\Delta\nu=\Gamma_0}$. Supposing that $\Gamma/\Gamma_0 \approx 1$ and $\alpha\beta < \Gamma_0$, $\Gamma(B)$ is then found to be

$$\Gamma(B) = \Gamma_0 + \frac{A(E_+^2 - E_-^2)}{4[A_0 E_0^2 + A(E_+^2 + E_-^2)]} \alpha B$$

$$+ \frac{A(E_+^2 + E_-^2)}{8[A_0 E_0^2 + A(E_+^2 + E_-^2)]} \frac{\alpha^2}{\Gamma_0} B^2, \quad (C9)$$

where B is in units of gauss and Γ is in units of megahertz. The formula (C9) only holds for a weak magnetic field B and a small change of the linewidth $(\Gamma - \Gamma_0 \ll \Gamma_0)$. Finding the offset Γ_0 in Fig. 6(a) by fitting $\Gamma(B)$ with respect to the variable B leads to finding the near-zero-B currents in the Helmholtz-coil system.

M. Allegrini, E. Arimondo, and L. A. Orozco, J. Phys. Chem. Ref. Data 51, 043102 (2022).

^[2] M. S. Safronova, D. Budker, D. DeMille, D. F. J. Kimball, A. Derevianko, and C. W. Clark, Rev. Mod. Phys. 90, 025008 (2018).

^[3] C.-H. Chu, P.-C. Chang, Y.-J. Shih, D.-A. Luh, M.-S. Chang, T.-W. Liu, B.-W. Chen, and W.-Y. Cheng, Opt. Lett. 48, 5984 (2023).

^[4] K.-H. Chen, C.-M. Wu, S.-R. Wu, H.-H. Yu, T.-W. Liu, and W.-Y. Cheng, Opt. Lett. 45, 4088 (2020).

- [5] P. Morzyński, P. Wcisło, P. Ablewski, R. Gartman, W. Gawlik, P. Masłowski, B. Nagórny, F. Ozimek, C. Radzewicz, M. Witkowski, R. Ciuryło, and M. Zawada, Opt. Lett. 38, 4581 (2013).
- [6] S. G. Porsev, K. Beloy, and A. Derevianko, Phys. Rev. D 82, 036008 (2010).
- [7] H. B. Tran Tan and A. Derevianko, Phys. Rev. A 107, 042809 (2023).
- [8] U. I. Safronova, M. S. Safronova, and W. R. Johnson, Phys. Rev. A 95, 042507 (2017).
- [9] A. Derevianko, Phys. Rev. A 65, 012106 (2001).
- [10] B. K. Sahoo, B. P. Das, and H. Spiesberger, Phys. Rev. D 103, L111303 (2021).
- [11] N. D. Lemke, K. W. Martin, R. Beard, B. K. Stuhl, A. J. Metcalf, and J. D. Elgin, Sensors 22, 1982 (2022).
- [12] M. Nakazawa, J. Appl. Phys. **59**, 2297 (1986).
- [13] C.-Y. Cheng, C.-M. Wu, G.-B. Liao, and W.-Y. Cheng, Opt. Lett. 32, 563 (2007).
- [14] C.-M. Wu, T.-W. Liu, and W.-Y. Cheng, Phys. Rev. A 92, 042504 (2015).
- [15] W.-Y. Cheng, T.-J. Chen, C.-W. Lin, B.-W. Chen, Y.-P. Yang, and H.-Y. Hsu, Opt. Express 25, 2752 (2017).
- [16] T.-J. Chen, J.-E. Chen, H.-H. Yu, T.-W. Liu, Y.-F. Hsiao, Y.-C. Chen, M.-S. Chang, and W.-Y. Cheng, Opt. Lett. 43, 1954 (2018)
- [17] F. Biraben, M. Bassini, and B. Cagnac, J. Phys. France 40, 445 (1979).
- [18] Number 019; 3 April 2024, 07:05 a.m.; magnitude:7.1. https://scweb.cwa.gov.tw/en-us/earthquake/details/ EE2024040307580971019.

- [19] F. W. Bell Technologies Inc., Model 5180 Hand-Held Gauss/Tesla meter.
- [20] W. Demtröder, Laser Spectroscopy, 3rd ed. (Springer, Berlin, 2003), Chap. 7, p. 482.
- [21] G. Grynberg, B. Cagnac, and F. Biraben, in Coherent Nonlinear Optics, edited by M. S. Feld and V. S. Letokhov (Springer, Berlin, 1980), p. 136.
- [22] https://jcgm.bipm.org/vim/en/2.41.html.
- [23] Rb rf clock calibrated by a Cs atomic-beam clock and a H clock, with drift 1.02×10^{-11} per week.
- [24] Symmetricom 5071a Cs clock, with accuracy 1.4×10^{-14} (1 day), 10^{-11} (10 s).
- [25] Aftershocks 17 April 2024 to 19 April 2024, Richter 4–1. https://scweb.cwa.gov.tw/en-us/earthquake/data.
- [26] N. Allard and J. Kielkopf, Rev. Mod. Phys. 54, 1103 (1982) (see, in particular, p.1159).
- [27] A. Kortyna, N. A. Masluk, and T. Bragdon, Phys. Rev. A 74, 022503 (2006).
- [28] L. Armstrong, Jr., *Theory of the Hyperfine Structure of Free Atoms* (Wiley, New York, 1971), Chap. IV.
- [29] M. Safronova, R. Eigenmann, B. Arora, P. Barakhshan, A. Kiruga, A. Marrs, A. Bhosale, C. Cheung, D. Filin, Cs 6D_{3/2} lifetime data (University of Delaware, Newark, 2024), https://www1.udel.edu/atom/transition?element=Cs1.
- [30] E. Arimondo, M. Inguscio, and P. Violino, Rev. Mod. Phys. 49, 31 (1977).
- [31] P. J. Mohr, D. B. Newell, B. N. Taylor, and E. Tiesinga, Rev. Mod. Phys. 97, 025002 (2025).